Astronomy & Astrophysics manuscript no. 26944
October 21, 2015
©ESO 2015

To Ba or not to Ba: Enrichment in s-process elements in binary systems with WD companions of various masses

T. Merle[1], A. Jorissen[1], S. Van Eck[1], T. Masseron[1,2], and H. Van Winckel[3]

[1] Institut d'Astronomie et d'Astrophysique, Université Libre de Bruxelles, CP 226, Boulevard du Triomphe, 1050 Brussels, Belgium
e-mail: tmerle@ulb.ac.be
[2] Institute of Astronomy, University of Cambridge, Madingley Road, Cambridge CB3 0HA, UK
[3] Instituut voor Sterrenkunde, Katholieke Universiteit Leuven, Celestijnenlaan 200D, 3200 Heverlee, Belgium

Received ...; accepted ...

arXiv:1510.05908v1 [astro-ph.SR] 20 Oct 2015

ABSTRACT

Context. The enrichment in s-process elements of barium stars is known to be due to pollution by mass transfer from a companion formerly on the thermally-pulsing asymptotic giant branch (AGB), now a carbon-oxygen white-dwarf (WD).
Aims. We are investigating the relationship between the s-process enrichment in the barium star and the mass of its WD companion. It is expected that helium WDs, which have masses smaller than about 0.5 $M_\odot$ and never reached the AGB phase, should not pollute with s-process elements their giant companion, which should thus never turn into a barium star.
Methods. Spectra with a resolution of $R \sim 86\,000$ were obtained with the HERMES spectrograph on the 1.2-m Mercator telescope for a sample of 11 binary systems involving WD companions of various masses. We use standard 1D LTE MARCS model atmospheres coupled with the Turbospectrum radiative-transfer code embedded in the BACCHUS pipeline to derive the atmospheric parameters using equivalent widths of Fe I and Fe II lines. Least-square minimization between the observed and synthetic line shape is used to derive the detailed chemical abundances of CNO and s-process elements.
Results. The abundances of s-process elements for the entire sample of 11 binary stars were derived homogeneously. The sample encompasses all levels of overabundances: from solar [s/Fe]= 0 to 1.5 dex in the 2 binary systems with S-star primaries (for which dedicated MARCS model atmospheres were used). The primary components of binary systems with a WD more massive than 0.5 $M_\odot$ are enriched in s-process elements. We also found a trend of increasing [s/Fe] with [C/Fe] or [(C+N)/Fe].
Conclusions. Our results conform to the expectation that binary systems with WD companions less massive than 0.5 $M_\odot$ do not host barium stars.

Key words. Stars: abundances – white dwarfs – Stars: late-type – binaries: spectroscopic

1. Introduction

The puzzle of the barium stars, a class of K giants with overabundances of heavy elements produced by the s-process of nucleosynthesis (Bidelman & Keenan 1951), has been solved by McClure et al. (1980) who unravelled the binary nature of these stars, with the companion endorsing the responsibility of the heavy-element synthesis. This solution of course requires the companion to be a carbon-oxygen white dwarf (WD), which synthesized the heavy elements while on the thermally-pulsing asymptotic giant branch (TP-AGB). An indirect argument supporting that hypothesis has been provided by McClure & Woodsworth (1990) and Jorissen et al. (1998) in the form of the mass-function distribution, consistent with the companion masses being peaked at 0.6 $M_\odot$, as expected for carbon-oxygen WDs. It is only quite recently that a clear *direct* argument was presented by Gray et al. (2011), in the form of the detection by GALEX of UV excess flux from those systems, attributable to a warm WD. Earlier studies by Schindler et al. (1982), Dominy & Lambert (1983), Böhm-Vitense et al. (1984); Böhm-Vitense et al. (2000), Jorissen et al. (1996), and Frankowski & Jorissen (2006) found similar evidence, although somewhat less convincingly or for a smaller set.

With the advent of sensitive far-UV and X-ray satellites, like EUVE, XMM-Newton and ROSAT, many warm WDs were discovered from their X-ray or UV flux (see Bilíková et al. 2010, and references therein). Some among these are members of binary systems involving a late-type primary star (e.g., Landsman et al. 1993; Vennes et al. 1995, 1997, 1998; Jeffries & Smalley 1996; Jorissen et al. 1996; Christian et al. 1996; Burleigh et al. 1997, 1998; Hoard et al. 2007; Bilíková et al. 2010), with the latter thus being barium-star candidates. Of course, for this to happen, the progenitor of the current WD had to be a TP-AGB star with an atmosphere enriched in s-process elements. This in turn requires that the s-process nucleosynthesis operated in the H- and He-burning intershell region *and* that the s-process material was dredged up to the surface. The currently available sample of WDs in binary systems offers an interesting way to test the above paradigm, especially when the mass of the WD is known. By checking whether or not the *current companion* of the WD is enriched in s-process elements, we may trace the operation of s-process and dredge-up in the AGB progenitor of the current WD. Since its mass is equivalent to the AGB core mass at the end of its evolution, we may thus set constraints on models of AGB evolution by investigating whether there is a threshold on the WD mass for its companion to become a barium star. It is expected for instance that He WDs, which are less massive than CO WDs, had progenitors which did not ascend the AGB. Their companion should thus never be barium stars. This was recently proven

to be true for the IP Eri system, whose K primary star, companion of a He WD, is not a barium star (Merle et al. 2014). The present paper addresses this issue on a larger sample of binaries involving WDs covering a broad range of masses.

The paper is organized as follows. Sect. 2 describes the stellar sample and Sect. 3 the observations. Sect. 4 presents the method used for deriving the atmospheric parameters, and Sect. 5 the resulting abundances, separately for CNO and s-process elements. Sects. 6 and 7 contain the discussion about these results, and our conclusions, respectively.

2. The sample

The binary systems selected for the present study have WD components orbiting a cool star (with $T_{\rm eff} < 7000$ K). The main selection criterion was the knowledge of the WD mass, which ranges from 0.3 to 1.0 $M_\odot$. Our sample is listed in Table 1. Incidentally, the sample covers a broad range of orbital periods and eccentricities. The WD masses are taken from the references listed in Table 1.

Here follow remarks on some targets of our sample.

IP Eri (HD 18131) consists of a K0 IV star and a He WD companion. Its evolutionary history has been studied by Siess et al. (2014), whereas an abundance study was performed by Merle et al. (2014).

14 Aur C (HD 33959) is member of a quadruple system with component A being a δ Scuti star. 14 Aur C is located 14.6 arcsec from A, at a distance of 104 ± 32 pc from the Sun (van Leeuwen 2007). Spectral types F2V+DA (Vennes et al. 1998) or F5V (Gray et al. 2003) have been proposed. It appears to be a fast rotator. We derived for this star $v \sin i = 16$ km s^{-1}. No atmospheric parameters are available yet in the literature for that star. The orbital period of only 3 d makes the dwarf star 14 Aur C an outlier among the period distribution of giant barium stars, but not among that of dwarf carbon stars (should 14 Aur C turn to be so), where at least one star with a similar period is known (HE 0024-2523 has a period of 3.4 d; Lucatello et al. 2003).

V1261 Ori (HD 35155) is a symbiotic S star (Ake et al. 1991; Jorissen et al. 1996).

IT Vir (HD 121447) is a border case between barium and S stars, since it has been classified as SC2 (Ake 1979), K4Ba (Abia & Wallerstein 1998), K7Ba and S0.

ζ Cap (HD 204075) is a prototype barium star.

DR Dra (HD 160538) and V1379 Aql (HD 185510) have strong emission cores in the Ca II H and K lines (Fig. 1), indicative of chromospheric activity related to rapid rotation, as confirmed by our analysis ($v \sin i = 8.5$ km s^{-1} and 18 km s^{-1}, respectively; see Fig. 3) in agreement with the results of Fekel et al. (1993). Emission is also visible in the IR Ca II triplet.

3. Observations

High-resolution spectra ($R \sim 86\,000$) were obtained using the HERMES spectrograph (Raskin et al. 2011) operating at the 1.2 m telescope Mercator at La Palma (Canary Islands, Spain). The HERMES spectrograph is a fiber-fed echelle spectrograph which provides a full spectral coverage from 377 to 900 nm. All the spectra were reduced using the HERMES pipeline software and have a typical signal-to-noise ratio of about 200. The observations were carried out between June 2009 and September 2014.

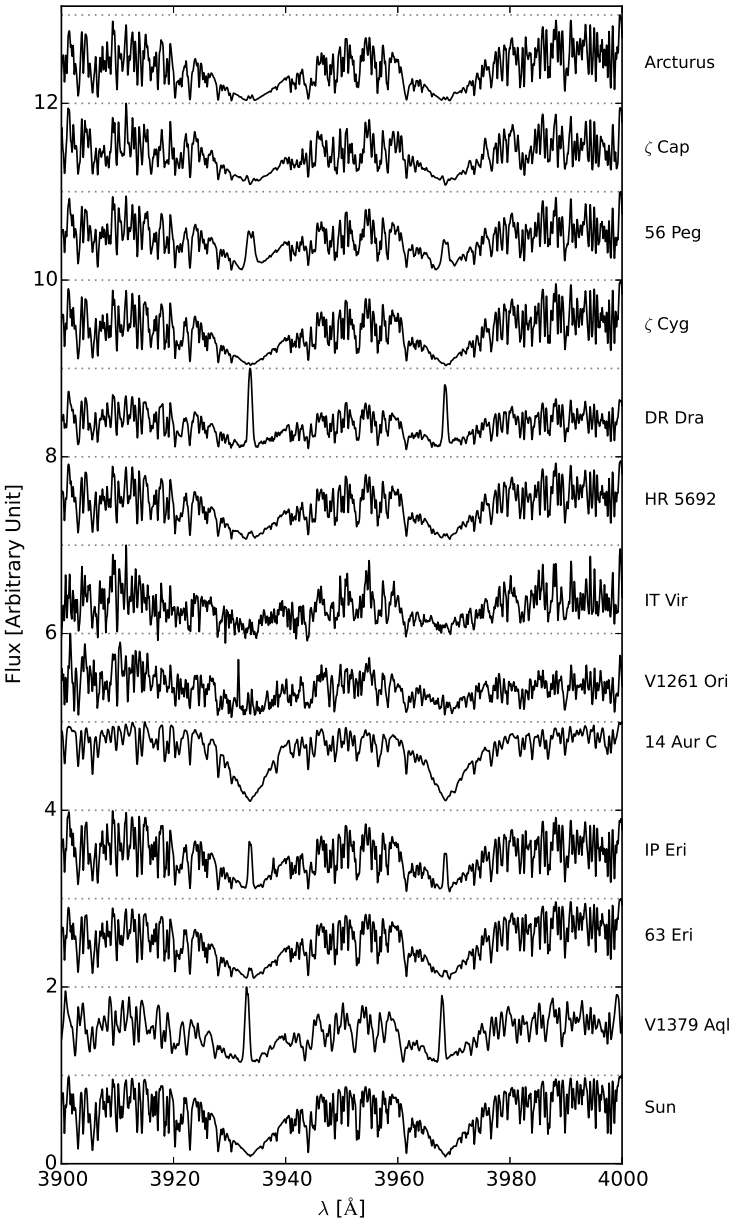

Fig. 1. The Ca II H and K lines for the sample stars. For comparison, the spectra of the Sun and Arcturus are plotted at the bottom and at the top of the figure, respectively. Evidence of activity is present in 63 Eri, IP Eri, V1379 Aql, DR Dra and 56 Peg.

4. Atmospheric parameters

First guesses for the atmospheric parameters were determined from previous works (as listed in Sect. 2), from photometry or spectral classification. We assume the metallicity to be solar to start with [the solar abundance set from Grevesse et al. (2007) has been used throughout this paper, with in particular $A_\odot$(Fe) = 7.45[1]].

The atmospheric parameters were then determined iteratively using the pipeline BACCHUS developed by one of the author (TMa; see also Jofre et al. 2013). This pipeline is based on the 1D LTE spectrum-synthesis code Turbospectrum (Alvarez & Plez 1998; Plez 2012) and the method to derive the atmospheric parameters is based on the fit of the equivalent

[1] defined as $A(\mathrm{Fe}) = \log[n(\mathrm{Fe})/n(\mathrm{H})] + 12$, where n(Fe) and n(H) are the number densities of Fe and H.

Table 1. The sample of binary systems with a WD companion and known orbital elements (P and e are the orbital period and eccentricity, respectively, and $f(M_1, M_2)$ is the mass function), ordered by increasing WD mass.

Names	Spectral type	M_{WD} ($M_\odot$)	P (d)	e	$f(M_1, M_2)$ ($M_\odot$)	Ref.
EUVE J0459-102 HR 1608 (63 Eri)	G4V + He WD	0.3	903 ± 5	0.30 ± 0.06	0.009 ± 0.003	2, 3
HD 185510 (V1379 Aql)	K0III + sdB	0.30 – 0.36	20.66187 ± 0.00058	0.094 ± 0.011	0.0042 ± 0.0002	1
EUVE J0254-053 HD 18131 (IP Eri)	K0 IV + He WD	0.4	1071.0 ± 1.8	0.25 ± 0.01	0.0036 ± 0.0001	4, 5
EUVE J0515+326 HD 33959C (14 Aur C)	F3V	0.53 – 0.69	2.99322 ± 0.00005	0	0.0079 ± 0.0002	3
EUVE J1732+74.2 HD 160538 (DR Dra)	K0III	0.55	903.8 ± 0.4	0.07 ± 0.03	0.0035 ± 0.0003	1, 17
HD 35155 (V1261 Ori)	S4,1	0.55 ± 0.05	640.7 ± 2.7	0.07 ± 0.03	0.032 ± 0.003	6, 7
1RXS J151824.6+203423 HR 5692	G8III Ba0.3	0.59 – 0.79	506.45 ± 0.18	0.3353 ± 0.0056	0.0112 ± 0.0003	6, 8
HD 121447 (IT Vir)	K7III Ba SC2	0.5 – 0.7	185.66 ± 0.07	0.0	0.025 ± 0.001	16
HD 202109 (ζ Cyg)	G8III Ba0.6	0.7 - 1.1	6489 ± 31	0.22 ± 0.03	0.023 ± 0.003	9, 10, 14
RX J2307.1+2528 HR 8796 (56 Peg)	K0Iab Ba	0.75 - 1.15	111.14 ± 0.01	0	$(3.7 \pm 0.3)\ 10^{-5}$	11, 12, 13
ζ Cap HD 204075	G4Ib Ba	1	2378 ± 55	0.28 ± 0.07	0.004 ± 0.001	14, 15

References. (1) Fekel et al. (1993); (2) Landsman et al. (1993); (3) Vennes et al. (1998) (4) Burleigh et al. (1997); (5) Merle et al. (2014); (6) Jorissen et al. (1996); (7) Jorissen et al. (1992); (8) Stefanik et al. (2011); (9) Dominy & Lambert (1983); (10) Griffin & Keenan (1992); (11) Schindler et al. (1982); (12) Griffin (2006); (13) Frankowski & Jorissen (2006); (14) Böhm-Vitense (1980); (15) Jorissen et al. (1998); (16) Jorissen et al. (1995); (17) Fekel & Simon (1985).

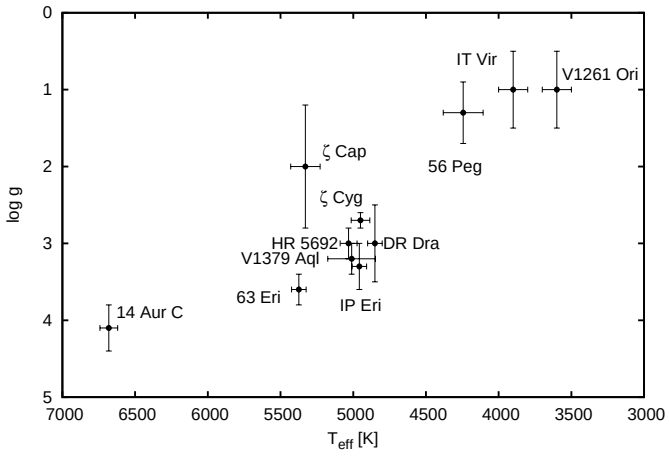

Fig. 2. Surface gravity vs effective temperature for the sample stars.

widths of Fe I and Fe II lines. The code derives automatically the effective temperature $T_{\rm eff}$, the logarithmic surface gravity $\log g$, the global metallicity [Fe/H] and the microturbulent velocity ξ by removing any trend in the [Fe/H] vs. χ and [Fe/H] vs. W/λ relations (where χ is the energy of the lower level of a line, W the measured equivalent width and λ the wavelength of the considered line), and by forcing lines of Fe I and Fe II to yield the same abundance. We used MARCS model atmospheres (Gustafsson et al. 2008) and a line list constructed from the VALD3 database (Kupka et al. 2011), complemented for Fe and V lines by data from Den Hartog et al. (2014b,a) and Ruffoni et al. (2014).

The synthetic spectra were convolved with a Gaussian function with a σ varying from 6 to 12 km s^{-1} to match the stellar macroturbulence and/or HERMES resolution. Only reduced equivalent widths (W/λ) of Fe I and Fe II lines lower than 0.025 are retained in the analysis. For the fast rotators 14 Aur C ($V \sin i$ = 16 km s^{-1}) and V1379 Aql ($V \sin i$ = 18 km s^{-1}), we convolved the synthetic spectra with a rotational profile.

Merle et al. (2014) performed an abundance analysis of IP Eri, and obtained the following atmospheric parameters: $T_{\rm eff} = 4960 \pm 100$ K, $\log g = 3.3 \pm 0.3$, and [Fe/H]= $+0.09 \pm 0.08$, which will be used here as well.

The atmospheric parameters of the prototypical Ba star ζ Cap ($T_{\rm eff}$ = 5397 ± 82 K, $\log g$ = 1.48 ± 0.16, and [Fe/H] = -0.14 ± 0.10) were derived by Prugniel et al. (2011). They were re-derived in the present study, and the two parameter sets are close to each other.

For the two S stars (IT Vir and V1261 Ori), the atmospheric parameters cannot be derived with BACCHUS due to the presence of strong molecular lines which blend many Fe lines and prevent the use of their equivalent widths. Instead, for V1261 Ori, we adopted the parameters derived by Neyskens et al. (2015) who took into account the specific chemical composition of S stars and its feedback on the model-atmosphere structure. A new grid of MARCS model atmospheres dedicated to S stars (Van Eck et al. 2011) has been used for that purpose.

Neyskens et al. (2015) obtained $T_{\rm eff}$ = 3600 K, $\log g$ = 1.0, [Fe/H]= −0.5, C/O= 0.5 and [s/Fe]= +1.0. These parameters will be adopted in the present study.

For IT Vir, a border case between Ba and S stars, Abia & Wallerstein (1998) estimated the atmospheric parameters to be $T_{\rm eff}$ = 4000 K, $\log g$ = 1.0, and [Fe/H] = −1.0 with ξ = 2 km s^{-1} and C/O= 0.95, while Smith (1984) had previously found $T_{\rm eff}$ = 4200 K, $\log g$ = 0.8, [Fe/H] = 0.05, and C/O= 0.79. The $V - K$ index ($V - K$ = 3.65) combined with the calibration of Bessell et al. (1998) yields $T_{\rm eff}$ = 3900 K. We adopted that value for the temperature combined with Abia & Wallerstein (1998) gravity.

The resulting atmospheric parameters are shown in Table 2, sorted by increasing effective temperatures (as in all the following tables). The uncertainties on the atmospheric parameters provided by the BACCHUS pipeline are those resulting from the propagation of the line-to-line Fe-abundance scatter on the trends used to derive the atmospheric parameters, as explained above. Uncertainties on $T_{\rm eff}$ lower than 50 K were arbitrarily set to a minimum value of 50 K.

5. Abundances

We have chosen to perform the abundance analysis using spectrum synthesis. The detailed abundance analysis was performed using the BACCHUS pipeline abundance module. Only the least blended lines were retained for the analysis. This selection was performed over the whole HERMES wavelength range (i.e., [370 − 890] nm). The atomic line list (Table A.1) includes the isotopic shifts for Ba II (with an update for isotopes 130 and 132) and the hyperfine structure for La II from Masseron (2006). The CH molecular line list is from Masseron et al. (2014) and CN is from Sneden et al. (2014). The references for the other molecular line lists (TiO, SiO, VO, C_2, NH, OH, MgH, SiH, CaH and FeH) can be found in Gustafsson et al. (2008). Line fitting is based on a least-square minimization method and all lines are visually inspected to check for possible issues (caused by, e.g., line blends, cosmic hits, ...). Results are presented in Table 3 for CNO abundances, and in Tables 4 and 5 for Sr, Y, Zr, Ba, La, and Ce. The uncertainties given in Tables 3 and 4 correspond to the standard deviation of the line-to-line dispersion, whereas in Table 5, the total uncertainties (thus including the impact of the uncertainties from the model parameters) are listed.

5.1. C, N, O abundances

C, N, and O abundances were derived in the following sequence: first O, then C and finally N. For deriving the oxygen abundance, we mainly used the [O I] 630.030 and 636.378 nm lines since the O I triplet resonance line at 777 nm is strongly affected by NLTE effects [see Asplund (2005) for a detailed discussion]. The O I triplet line yields a LTE abundance larger by about ∼ 0.2 − 0.4 dex as compared to the abundance derived from the forbidden lines. This is not the case for the star 63 Eri, however, since for that star, the triplet and the strong doublet at 844.636 and 844.676 nm give consistent abundances within 0.04 dex, even though the [O I] 630.030 nm is blended with a telluric line in its blue wing (which has not been considered in the fit procedure thus). This star has one of the largest gravity, leading to a decrease of the non-LTE effects on the 777 nm triplet. For 14 Aur C, the two forbidden lines are lost in the noise, so that we use instead the highly excited, very weak line at 615.68 nm.

Although it is particularly difficult to find unblended atomic lines of C I, we found 5 useful weak lines (as listed in Table A.1), except in V1379 Aql, V1261 Ori and IT Vir where they are not visible or too blended to be useful. This is why we prefer to use lines of diatomic carbon C_2 for deriving carbon abundances. Lines of C_2 appear roughly between 400 and 600 nm. In the molecular linelists, we first identified useful lines of C_2 by comparing synthetic spectra (for typical values of the atmospheric parameters) with only C_2 lines included and with all lines included to identify the least blended C_2 lines. Then by comparing with observed spectra, we ended up with a selection of ∼20 lines (Table B.1) visible in at least two-thirds of the objects. The line at 513.56 nm used by Barbuy et al. (1992) is also included. Good fits of C_2 bands are difficult to achieve but the lines are so sensitive to the carbon abundance that the latter can be easily inferred even from rough fits. In 14 Aur C, rotation broadens the lines so much (see Fig. 3) that only three lines, despite being blended with others, can nevertheless be used to derive the carbon abundance. Especially the C_2 line at 468.427 nm appears useful for this star (it is not used for the other stars because the line position in the synthetic spectrum appears to be somewhat redder than observed). The C/O ratio is then calculated and listed in Table 3.

We selected ten N I lines (Table A.1). But for the range of atmospheric parameters under consideration, N I lines are always very weak and blended with CN lines. The N abundance thus combines N I and CN lines, using the carbon abundance from the previous step. The CN lines are numerous and span the full HERMES spectral range. We selected 121 CN lines unblended or weakly blended, in the range 640 to 890 nm (Table B.1). All CN lines are eye-checked because a lot of telluric lines are present in this wavelength range and can strongly blend with CN lines. Below 500 nm, CN lines are too much blended by atomic and molecular features (mainly from CH, C_2, MgH, and SiH) to be of any use. NH lines cannot be used because they are located beyond the violet edge of the spectrograph (370 nm). For the fast rotator 14 Aur C, almost no CN lines can be used, since weak lines blend together due to rotational broadening. We nevertheless used 2 lines among the selected CN lines, plus 2 other weak lines not in the original selection (at ∼ 871.15 and 871.88 nm). The N abundance in 14 Aur C is uncertain since the weak lines are at the limit of the spectral noise.

The S star V1261 Ori requires a specific way to derive its carbon abundance since atomic and C_2 lines are flooded in TiO and ZrO bands. Infrared bands from CO, CN and OH around 2 μm must be used instead, as done by Smith & Lambert (1990) (with atmospheric parameters $T_{\rm eff}$ = 3650 K, $\log g$ = 0.8, [Fe/H] = −0.52). We therefore used their CNO values for determining the subsequent s-process elements.

The derivation of CNO abundances in IT Vir is particularly challenging and consistently leads to a [N/Fe] ratio above 1.0 dex. We proceeded as follows: we first estimated the O abundance through the [O I] 630.0 nm line using spectral syntheses computed from dedicated S-star model atmospheres with the parameters listed in Table 2, and three different values of the C/O ratio (0.50, 0.75 and 0.90). Basically, as the C/O ratio increases (for a given O abundance), the strength of the forbidden line decreases. This strength is well reproduced for [O/Fe] = +0.20, +0.40 and +0.60 dex, respectively. Then, for each C/O ratio and the corresponding O abundance, a carbon abundance ensues. We checked which one among these carbon abundances best fit the C_2 lines (between 460 and 560 nm) but we could only exclude the value corresponding to C/O = 0.5; the other two possibilities leading to similarly good fits, they could not be discriminated. From the above analysis, we can at least be sure that the C/O ratio is intermediate between the solar value and unity, thus

Table 2. Spectroscopic stellar parameters derived with BACCHUS. Stars are ordered according to increasing $T_{\rm eff}$.

Star name	HD	$T_{\rm eff}$ (K)	$\log g$	[Fe/H]	ξ (km s^{-1})
V1261 Ori[a]	35155	3600 ± 100	1.0 ± 0.5	−0.5 ± 0.5	2.0 ± 0.5
IT Vir[a]	121447	3900 ± 100	1.0 ± 0.5	−0.5 ± 0.5	2[b]
56 Peg	218356	4244 ± 137	1.3 ± 0.4	−0.45 ± 0.12	1.55 ± 0.06
DR Dra	160538	4851 ± 50	3.0 ± 0.5	−0.14 ± 0.10	1.76 ± 0.05
ζ Cyg	202109	4950 ± 64	2.7 ± 0.1	−0.03 ± 0.08	1.43 ± 0.03
IP Eri	18131	4958 ± 50	3.3 ± 0.3	0.09 ± 0.08	1.45 ± 0.04
V1379 Aql	185510	5011 ± 164	3.2 ± 0.2	−0.23 ± 0.12	1.68 ± 0.17
HR 5692	136138	5032 ± 58	3.0 ± 0.2	−0.08 ± 0.09	1.35 ± 0.04
ζ Cap	204075	5329 ± 101	2.0 ± 0.8	−0.08 ± 0.13	2.26 ± 0.05
63 Eri	32008	5374 ± 50	3.6 ± 0.2	−0.18 ± 0.08	1.03 ± 0.04
14 Aur C	33959 C	6681 ± 61	4.1 ± 0.3	−0.11 ± 0.08	1.75 ± 0.09

Notes. [(a)] Atmospheric parameters not determined with BACCHUS [(b)] No uncertainty given by Abia & Wallerstein (1998) from whom this value has been adopted

Table 3. C, N, and O abundances. Only the statistical uncertainties are given here. The number of lines used are between parentheses.

Star	[Fe/H]	[C/Fe]	[N/Fe]	[O/Fe]	C/O
V1261 Ori[a]	−0.66 ± 0.09	0.39 ± 0.14[1]	0.73 ± 0.11[2]	0.54 ± 0.08[3]	0.38
IT Vir[b]	−0.45 ± 0.25	0.55	1.39 ± 0.30 (50)	0.40 (1)	0.75
		0.62	1.11 ± 0.20 (94)	0.60 (1)	0.90
56 Peg	−0.45 ± 0.12	0.01 ± 0.23 (13)	−0.17 ± 0.07 (82)	0.12 ± − (1)	0.63
DR Dra	−0.14 ± 0.10	−0.23 ± 0.07 (8)	−0.21 ± 0.09 (82)	0.15 ± − (1)	0.39
ζ Cyg	−0.03 ± 0.08	−0.22 ± 0.13 (15)	0.11 ± 0.05 (94)	0.16 ± 0.06 (2)	0.44
IP Eri	0.09 ± 0.08	−0.14 ± 0.16 (18)	−0.23 ± 0.06 (96)	0.14 ± − (1)	0.54
V1379 Aql	−0.23 ± 0.12	−0.24 ± 0.13 (8)	0.21 ± 0.05 (29)	–	–
HR 5692	−0.08 ± 0.09	−0.24 ± 0.10 (10)	−0.16 ± 0.08 (90)	0.20 ± − (1)	0.43
ζ Cap	−0.08 ± 0.13	0.11 ± 0.05 (16)	0.38 ± 0.07 (85)	0.12 ± 0.08 (2)	0.79
63 Eri	−0.18 ± 0.08	−0.12 ± 0.18 (13)	0.25 ± 0.05 (50)	0.31 ± 0.04 (6)	0.20
14 Aur C	−0.11 ± 0.08	0.22 ± 0.03 (3)	0.25 ± 0.13 (4)	0.16 ± − (1)	0.72

Notes. [(a)] For this star, we used the Fe abundance from Kovacs (1983) scaled to the solar value of Holweger (1979). CNO abundances are from Smith & Lambert (1990) and are relative to α Tau [(b)] Two equally-likely abundance sets are listed for IT Vir (see text). [(1)] from CO lines at 1.6 and 2.2 μm [(2)] from CN lines at 2.2 μm [(3)] from OH lines at 1.6 and 2.2 μm

disqualifying the SC spectral type quoted in the literature. For each remaining pair of (C/O, [O/Fe]) values, we finally compute synthetic spectra for three different [N/Fe] values (0.0, +1.0 and +1.5 dex) and evaluate how well these synthetic spectra fit the observed spectrum in the three wavelength ranges [629 – 631], [776.5 – 778.5], and [843.5 – 845.5] nm containing CN lines. Good fits are obtained for [N/Fe] = 1.5 dex when C/O= 0.75, [O/Fe] = 0.40 dex and for [N/Fe] = 1.0 dex when C/O= 0.90, [O/Fe] = 0.60. Again, we cannot discriminate between these two equally good fits. Therefore both possibilities are listed in Table 3. Nevertheless, whenever necessary in the remainder of the study, we will adopt the former set.

We checked the sensitivity to gravity $\log g$ of our conclusion of a large N overabundance. Adopting $\log g$ = 0 instead of 1 as above, all other parameters being equal (with C/O= 0.75), we obtain a value of [N/Fe] still larger than 1.0. Similarly, increasing the temperature does not permit to lower the [N/Fe] value below 1.0 dex. We believe therefore that this result is robust.

5.2. s-process abundances

Atomic lines were carefully selected over the whole HERMES spectral range using both synthetic and observed spectra. They are listed in Table A.1. Whenever possible, for each species, we tried to select lines from both neutral and singly-ionized states (excluding strong resonance lines of neutral species known to suffer from NLTE effects).

The only observable lines of Sr II are the strong ones below 430.5 nm which are too strongly blended to derive reliable abundances. We therefore only used Sr I lines. Among the 8 selected Sr I lines, the line at 687.83 nm is often blended by telluric O_2, the resonance line at 460.73 nm is known to suffer from NLTE effects and to give abundances lower than that from higher excitation lines. The line at 707.01 nm has been used in all the target stars but 14 Aur C and V1261 Aur. In 14 Aur C, the two lines at 640.85 and 707.01 nm are not observable because they blend with other lines due to rapid rotation or are lost in the noise. Instead, the strong Sr II line around 416 nm seems to provide a reliable estimate of the Sr abundance. In V1261 Ori, the two Sr I

Table 4. Absolute s-process element abundances $A(X)$ (defined as $A(X) = \log[n(X)/n(H)] + 12$, where $n(X)$ and $n(H)$ are the number densities of X and H). Only the statistical uncertainties are given here. The number of lines used are between parentheses.

Star	A(Sr)	A(Y)	A(Zr)	A(Ba)	A(La)	A(Ce)
V1261 Ori	–	2.66 ± 0.27 (3)	3.48 ± 0.17 (4)	3.02 ± 0.32 (3)	1.91 ± 0.06 (2)	2.33 ± 0.07 (7)
IT Vir	3.44 ± – (1)	2.70 ± 0.12 (3)	3.99 ± 0.26 (7)	4.05 ± 0.18 (3)	2.42 ± 0.23 (4)	2.52 ± 0.20 (8)
56 Peg	3.05 ± 0.06 (2)	2.22 ± 0.22 (8)	2.44 ± 0.07 (7)	3.18 ± 0.18 (3)	1.12 ± 0.09 (8)	1.41 ± 0.09 (6)
DR Dra	3.04 ± 0.05 (2)	2.13 ± 0.22 (5)	2.77 ± 0.06 (5)	2.46 ± 0.08 (4)	1.17 ± 0.10 (8)	1.56 ± 0.07 (4)
ζ Cyg	3.33 ± – (1)	2.61 ± 0.16 (7)	2.96 ± 0.20 (9)	3.16 ± 0.25 (4)	1.52 ± 0.08 (9)	1.87 ± 0.12 (11)
IP Eri	3.14 ± – (1)	2.06 ± 0.12 (9)	2.86 ± 0.20 (7)	2.53 ± 0.09 (3)	1.25 ± 0.17 (6)	1.60 ± 0.09 (4)
V1379 Aql	2.89 ± – (1)	2.23 ± 0.04 (4)	2.59 ± 0.02 (2)	2.29 ± 0.07 (3)	1.11 ± 0.05 (3)	1.52 ± 0.16 (3)
HR5692	3.16 ± – (1)	2.63 ± 0.20 (6)	3.14 ± 0.19 (11)	2.90 ± 0.07 (5)	1.49 ± 0.10 (11)	1.77 ± 0.13 (9)
ζ Cap	3.86 ± 0.06 (2)	3.50 ± 0.21 (9)	3.87 ± 0.28 (11)	4.06 ± 0.13 (3)	2.09 ± 0.10 (11)	2.47 ± 0.15 (10)
63 Eri	2.84 ± 0.01 (2)	2.06 ± 0.13 (10)	2.48 ± 0.17 (8)	2.64 ± 0.22 (4)	1.15 ± 0.06 (10)	1.55 ± 0.06 (9)
14 Aur C	3.04 ± 0.05 (3)	2.03 ± 0.12 (7)	2.64 ± 0.07 (5)	2.60 ± 0.16 (4)	1.22 ± 0.11 (5)	1.50 ± 0.20 (3)
Sun[a]	2.92 ± 0.05	2.21 ± 0.02	2.58 ± 0.02	2.17 ± 0.07	1.13 ± 0.05	1.70 ± 0.10

Notes. [(a)] Solar abundances from Grevesse et al. (2007).

Table 5. Abundances of s-process elements. Total uncertainties are given here.

Star	[Sr/Fe]	[Y/Fe]	[Zr/Fe]	[Ba/Fe]	[La/Fe]	[Ce/Fe]	[s/Fe]
V1261 Ori	-	1.11 ± 0.58 (3)	1.56 ± 0.54 (4)	1.51 ± 0.62 (3)	1.44 ± 0.54 (2)	1.29 ± 0.24 (7)	1.38 ± 0.18
IT Vir	0.97 ± 0.26 (1)	0.94 ± 0.30 (3)	1.86 ± 0.38 (7)	2.33 ± 0.35 (3)	1.74 ± 0.39 (4)	1.27 ± 0.37 (8)	1.52 ± 0.55
56 Peg	0.58 ± 0.16 (2)	0.46 ± 0.28 (8)	0.31 ± 0.17 (7)	1.46 ± 0.28 (3)	0.44 ± 0.24 (8)	0.16 ± 0.24 (6)	0.57 ± 0.46
DR Dra	0.26 ± 0.14 (2)	0.60 ± 0.27 (5)	0.33 ± 0.16 (5)	0.43 ± 0.22 (4)	0.18 ± 0.23 (8)	0.00 ± 0.22 (4)	0.21 ± 0.16
ζ Cyg	0.34 ± 0.12 (1)	0.42 ± 0.22 (7)	0.39 ± 0.24 (9)	0.89 ± 0.31 (4)	0.40 ± 0.22 (9)	0.21 ± 0.24 (11)	0.49 ± 0.28
IP Eri	0.13 ± 0.12 (1)	−0.24 ± 0.19 (9)	0.19 ± 0.24 (7)	0.27 ± 0.21 (3)	0.03 ± 0.26 (6)	−0.19 ± 0.22 (4)	0.03 ± 0.21
V1379 Aql	0.20 ± 0.15 (1)	0.25 ± 0.18 (4)	0.24 ± 0.16 (2)	0.35 ± 0.22 (3)	0.21 ± 0.23 (3)	0.05 ± 0.27 (3)	0.22 ± 0.10
HR5692	0.32 ± 0.12 (1)	0.50 ± 0.25 (6)	0.64 ± 0.23 (11)	0.81 ± 0.21 (5)	0.44 ± 0.23 (11)	0.15 ± 0.24 (9)	0.48 ± 0.23
ζ Cap	1.02 ± 0.17 (2)	1.37 ± 0.28 (9)	1.37 ± 0.33 (11)	1.97 ± 0.25 (3)	1.04 ± 0.25 (11)	0.85 ± 0.27 (10)	1.27 ± 0.40
63 Eri	0.10 ± 0.12 (2)	0.03 ± 0.20 (10)	0.08 ± 0.22 (8)	0.65 ± 0.29 (4)	0.20 ± 0.21 (10)	0.03 ± 0.21 (9)	0.18 ± 0.24
14 Aur C	0.23 ± 0.13 (3)	−0.07 ± 0.19 (7)	0.17 ± 0.15 (5)	0.54 ± 0.25 (4)	0.20 ± 0.23 (5)	−0.09 ± 0.29 (3)	0.16 ± 0.23

lines at 640.85 and 707.01 nm are too blended and we used instead two Sr I lines at 687.83 and 689.26 nm even though the continuum placement remains the largest uncertainty.

For Y, we mainly used clean lines of Y II that are more numerous than Y I lines. The cleanest and most useful Y II lines in our sample are located at 528.98, 540.28, 572.89, and 679.54 nm. The other lines used are listed in Appendix A.

For Zr, we mainly used lines of Zr I, since they are more numerous than Zr II lines. Lines of Zr I between 800 and 850 nm, when useful, give abundances systematically stronger, by about ∼ 0.5 dex. For 14 Aur C, only Zr II lines below 540 nm can be used for the abundance determination. Since V1261 Ori is veiled by ZrO molecular bands, we used the same lines (between 740 and 758 nm) as those used by Smith & Lambert (1990) to derive the Zr abundance. Lines above 800 nm are useable but give somewhat higher abundances, as already mentioned.

For s-process elements belonging to the second peak (Ba, La and Ce), only neutral lines are available for Ba. We do not use the Ba II resonance lines at 455.4 and 493.4 nm in the abundance analysis due to known NLTE effects (see e.g., Olshevsky & Shchukina 2007), except in 14 Aur C where too few other lines are available. We mainly use the Ba II lines at 585.37, 614.17, 649.69 nm and the Ba I line at 748.81 nm.

Many lines (about 30) are available for La and Ce in the HERMES wavelength range. The most useful La II lines are located at 529.08, 530.20, 530.35, 617.27, 639.05, and 677.43 nm. The most useful Ce II lines are located at 456.24, 533.06, 604.34, 802.56, 871.67, and 877.21 nm. The Ce II lines are the strongest in V1261 Ori, which indeed has the largest Ce overabundance ([Ce/Fe] = 1.29 dex) in our sample.

To illustrate the good agreement between observed and synthetic spectra, we show in Fig. 3 the spectral region around the Ba II 585.36 nm line, which is well visible in the entire sample. The synthetic spectra in blue are computed with [Ba/Fe] = 0 whereas the red ones are computed with the appropriate [Ba/Fe] abundances as listed in Table 5. The red synthetic spectra reproduce nicely the observed spectra, especially for the fast rotators V1379 Aql and 14 Aur C. The fit is a bit worse for the cooler S stars V1261 Ori and IT Vir because of the presence of numerous

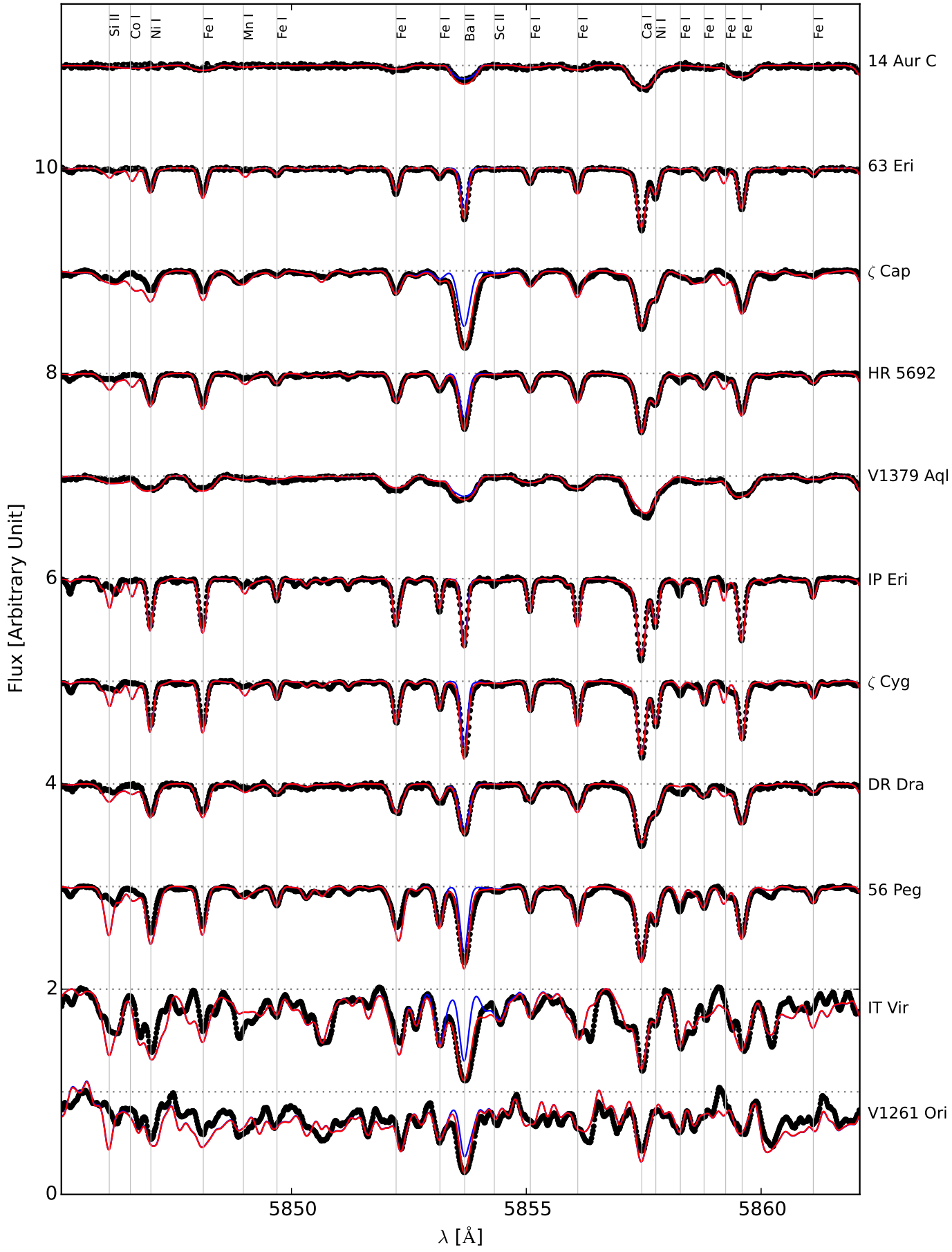

Fig. 3. Example of the observed and synthetic spectra around the Ba II line at 585.36 nm. The solid blue line corresponds to [Ba/Fe] = 0.

Table 6. The uncertainties on the derived abundances in ζ Cyg: σ_i are the uncertainties caused by the errors on the atmospheric parameters ($i = T_{\rm eff}$, $\log g$, [Fe/H], ξ; see text) and $\sigma_{\rm stat}$ is the line-to-line scatter on the abundance divided by $\sqrt{N}$, where N is the number of lines used. The individual model-driven uncertainties are quadratically added to yield the total model-driven uncertainty $\sigma_{\rm atm}$, which in turn is quadratically added to the statistical uncertainty to give the total uncertainty $\sigma_{\rm tot}$.

X	N	$\sigma_{T_{\rm eff}}$	$\sigma_{\log g}$	$\sigma_{\rm [Fe/H]}$	σ_ξ	$\sigma_{\rm atm}$	$\sigma_{\rm stat}$	$\sigma_{\rm tot}$
Sr	1	0.05	0.01	0.01	0.01	0.05	-	0.05
Y	7	0.03	0.10	0.01	0.04	0.11	0.06	0.13
Zr	9	0.09	0.01	0.01	0.01	0.09	0.07	0.12
Ba	4	0.09	0.09	0.06	0.05	0.15	0.11	0.19
La	9	0.03	0.16	0.03	0.01	0.17	0.03	0.17
Ce	11	0.03	0.14	0.05	0.02	0.15	0.04	0.16

molecular lines, but it is nevertheless possible to derive reliably the Ba abundance.

5.3. Uncertainties on s-process abundances

We investigated the impact on the s-process abundances of the uncertainties from the atmospheric parameters, adopting as typical uncertainties on these parameters (Table 2) the values $\sigma_{T_{\rm eff}} = \pm 50$ K, $\sigma_{\log g} = \pm 0.3$ dex, $\sigma_{\rm [Fe/H]} = \pm 0.10$ dex and $\sigma_\xi = \pm 0.10$ km s^{-1}.

The statistical uncertainty $\sigma_{\rm stat}$ listed in Table 6 is the line-to-line dispersion divided by $\sqrt{N}$, where N is the number of lines used for a given element (Table 6). This statistical uncertainty takes into account not only uncertainties on atomic data but also on continuum location and line-profile mismatch issues.

Statistical ($\sigma_{\rm stat}$) and model-induced (i.e., $\sigma_{T_{\rm eff}}$, $\sigma_{\log g}$, $\sigma_{\rm [Fe/H]}$ and σ_ξ) uncertainties are quadratically added (thus assuming independence between them, as is common practice, although in reality they may be correlated, as discussed by Johnson 2002) to obtain the total uncertainty $\sigma_{\rm tot}$ for each *s*-process element (which may thus be overestimated). We perform this analysis on ζ Cyg as it is representative of the whole sample (see Fig. 2). The estimated uncertainties are given in Table 6. Note that the uncertainties on the absolute s-process abundances given in Table 4 are only the line-by-line dispersion.

To get the uncertainties on the various [X/Fe] abundances (as listed in Table 5), we add quadratically the uncertainties on the absolute abundances A(Fe) and A(X) (as defined in footnote 1). The resulting uncertainties are expressed as:

$$\sigma_{\rm X} = \sqrt{\sigma_{\rm tot}({\rm X})^2 + \sigma({\rm Fe})^2 + \sigma_\odot({\rm X})^2 + \sigma_\odot({\rm Fe})^2} \quad (1)$$

where $\sigma_\odot$(X) denotes the uncertainty on the solar abundance of species X as given by Grevesse et al. (2007). The corresponding $\sigma_{\rm X}$ uncertainties are listed in Table 5 and plotted on Figs. 4 and 5.

5.4. Comparison with previous studies

V1261 Ori (HD 35155). That star has been analysed by Smith & Lambert (1990), who find the second-peak s-process elements (Ba, La, Ce, Nd) to be enriched by more than 1 dex, as we do. However, Smith & Lambert (1990) find no overabundance in excess of 0.23 dex for Y and Zr, whereas we find these elements to be overabundant by more than 1 dex. We stress that both the models and the line data are very different between the two studies.

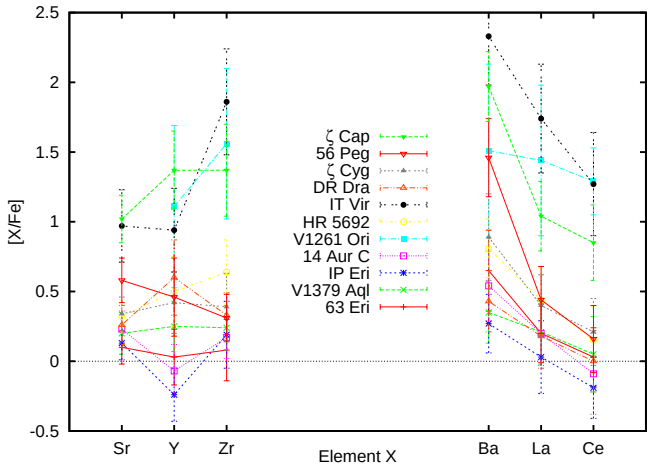

Fig. 4. First-peak (Sr, Y, Zr) and second-peak (Ba, La, Ce) s-process abundances relative to Fe.

IT Vir. Smith (1984) derived the CNO abundances in IT Vir, but does not confirm the large N abundance that we obtain for that star ([N/Fe] = 1.1 to 1.4 dex – Table 3– , as compared to 0.52 dex for Smith 1984). This large N overabundance goes along with a small ^{12}C/^{13}C ratio of 8 (Smith 1984), which could hint at CN processing. However, similarly small ^{12}C/^{13}C ratios are a common feature among barium stars (Smith 1984; Barbuy et al. 1992), without being associated with N overabundances as large as the one we find for IT Vir. We found that, whatever effective temperature or gravity is adopted for this star ($T_{\rm eff}$ = 3900 or 4200 K, $\log g$ = 0 or 1 dex; see Sect. 4), the large [N/Fe] overabundance remains. Even after carefully re-deriving O and C abundances, [N/Fe] is still larger than 1 dex. Formerly, the largest N abundances observed in barium stars were [N/Fe] = 0.7 dex in HD 27271 and 0.65 dex in HD 60197 (Barbuy et al. 1992). It may be relevant here to note that IT Vir has one of the largest Roche-lobe filling factor among barium stars, since it has a moderately short orbital period (186 d), but a comparatively large radius ($\sim$ 55 R$_\odot$; Jorissen et al. 1995). As a consequence, these authors report ellipsoidal variations for that star. The associated faster rotation, tidal deformations and departure from spherical symmetry will trigger meridional currents and deep mixing, and the observed large N abundance in IT Vir could perhaps be related to such processes currently occurring in the red giant (see for instance Decressin et al. 2009, for a discussion of rotation-induced mixing, and the resulting surface enhancement in nitrogen).

Regarding s-process abundances, the agreement is good for Sr, Y, and Ce, but Zr, Ba, and La are found to be more abundant by about 1 dex in our study as compared to Smith (1984).

56 Peg. It is the first time that an s-process abundance analysis is performed for 56 Peg, and it confirms its barium nature. Because of 56 Peg high luminosity (it is classified as K0Iab – confirmed by the low gravity of $\log g$ = 1.3; Table 2), one may have feared that the increased strength of the Ba II lines, which led to its classification as a barium star, were caused by the low atmospheric pressure, a consequence of Saha equation. But that fear is unjustified, since the present abundance analysis reveals a weak albeit definite s-process enhancement.

ζ Cap and ζ Cyg. These stars were analysed by Smiljanic et al. (2007). The agreement between the two studies on the s-process

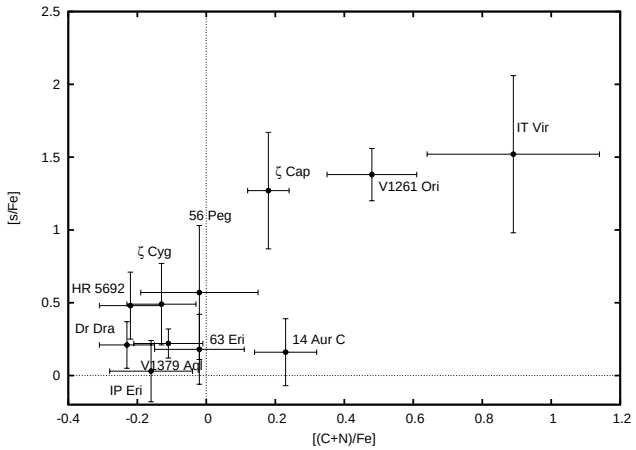

Fig. 6. The correlation between the s-process abundances and the carbon + nitrogen abundances.

abundances is reasonable (in particular, both studies find large overabundances in ζ Cap and much milder ones in ζ Cyg), except for Sr in ζ Cap: Smiljanic et al. (2007) obtain [Sr/Fe] = 2.21, as compared to 1.02 in the present study. Smiljanic et al. (2007) used the single Sr I resonance line at 460.73 nm, whereas we used that line and a line at 707.01 nm. Based solely on the 460.73 nm line, we find [Sr/Fe] = 0.99, and that value is in good agreement with the value 1.07 based on the 707.01 nm line. The reason for the discrepancy between the Sr abundances derived from the Sr I resonance line at 460.73 nm here and in Smiljanic et al. (2007) must partly reside in the different $\log gf$ values used [0.069 by Smiljanic et al. (2007) against 0.283 in our work, from NIST with the AA accuracy – see Appendix A], and partly in the different atmospheric parameters adopted.

DR Dra. Berdyugina (1994), Zacs et al. (1997), and Barisevičius et al. (2010) conclude, like we do, that DR Dra does not exhibit any s-process overabundance.

IP Eri. That star has been analyzed by Merle et al. (2014). We have rederived the s-process abundances with the same pipeline and methodology, but with a refined line selection for each element. The rederived s-process abundances agree with our previous work within the error bars and we obtain in the present study lower statistical uncertainties.

6. Discussion

The s-process abundance distribution is presented in Fig. 4 where it is clearly apparent that our sample contains both normal stars and stars enriched in s-process elements (and the latter also exhibit enhanced carbon and sometimes nitrogen overabundances; Fig. 6). The origin of the difference between these two stellar categories is clearly revealed when plotting the average s-process abundance, as listed in the last column of Table 5, as a function of the mass of the WD companion (Fig. 5). The expected trend is indeed obtained: s-process overabundances are found in those binary stars with a companion WD mass larger than about 0.5 $M_\odot$, i.e., the progenitor of the WD went through the thermally-pulsing AGB (TP-AGB) phase, was able to synthesize s-process elements in the intershell zone, and these were subsequently dredged up to the surface. Indeed, Hurley et al. (2000) (their Eq. 66) predict the minimum CO core mass at the base of the AGB (just at the end of core He-burning) to be at least 0.51 $M_\odot$ (for a star of initial mass 0.9 $M_\odot$). Conversely, when the WD mass is smaller than 0.51 $M_\odot$, the s-process synthesis did not occur (because the progenitor did not reach the TP-AGB): s-process overabundances are not observed. There are two marginal cases, namely DR Dra and 14 Aur C, whose WD mass qualifies them for being polluted by s-process material, but which are not. For 14 Aur C, apart from the difficulty imprinted on the analysis by the star rapid rotation, the cause for the absence of s-process enrichment could be its unusually short-period of 3 days, which is likely the outcome of a common-envelope evolution (Han et al. 1995). It is believed that this channel does not lead to substantial accretion during the common-envelope process (Ricker & Taam 2008)[2]. Nevertheless, the recent occurence of binary interaction is revealed by the rapid rotation of the star. The same holds true for DR Dra, whose absence of s-process overabundance is a bit more puzzling, however. The long period of DR Dra (904 d) suggests that the rapid rotation responsible for the chromospheric activity be due to spin accretion (Theuns et al. 1996) rather than to tidal coupling, which requires a closer system (Fekel et al. 1993). Thus there has been some binary interaction in the recent past of DR Dra. The absence of s-process overabundance in that star suggests that, with a mass estimated at 0.55 $M_\odot$ (Fekel & Simon 1985), either the WD does not originate from a TP-AGB star (Hurley et al. 2000), or there was no dredge-up in the TP-AGB star, or there was simply no s-process nucleosynthesis operating.

Among barium stars themselves, the level of s-process overabundances varies greatly, from the maginal level of HR 5692, ζ Cyg, and 56 Peg, to the largest level of IT Vir. Two co-existing causes for these variations are readily identified in the literature: on the one hand, the efficiency of the s-process nucleosynthesis in AGB stars varies with metallicity (Clayton 1988; Käppeler et al. 2011) and on the other hand, the efficiency of mass accretion varies with orbital separation (Jorissen & Boffin 1992; Han et al. 1995; Pols et al. 2003). Thus, orbital separation and metallicity could directly control the level of s-process overabundances in barium stars. But all previous studies have concluded that if any, the correlation between orbital periods and s-process overabundances is weak, and the present study is no exception. For instance, 56 Peg has one of the shortest orbital periods[3] among barium stars (111 d; Griffin 2006) and yet its s-process overabundance level is very moderate. A search for extra parameters (besides metallicity) blurring the relationship between orbital periods and s-process pollution levels is therefore of interest. Here we suggest that the WD mass, tracing the maximum luminosity reached on the AGB (through the core-mass – luminosity relationship; Herwig et al. 1998), could also play a role in that respect. Indeed, the AGB luminosity is a proxy for the number of thermal pulses experienced by the AGB star (although the initial AGB mass must play a role as well), which in turn governs the s-process level attained in its atmosphere. However, the number of stars available is still too scarce to be able to draw any firm conclusion, apart from the observation that large s-process overabundance levels are found at both ends of the CO WD mass range: around 0.6 $M_\odot$ (IT Vir, V1261 Ori) and around 1 $M_\odot$ (ζ Cap).

[2] The low-metallicity carbon dwarf HE 0024-2523, with its 3.4 d orbital period and its strong Pb overabundance, is a noticeable counter-example of this statement, though (Lucatello et al. 2003).

[3] We implicitly assume here that the range of system masses is moderate enough for orbital periods to be a good proxy for the orbital separations.

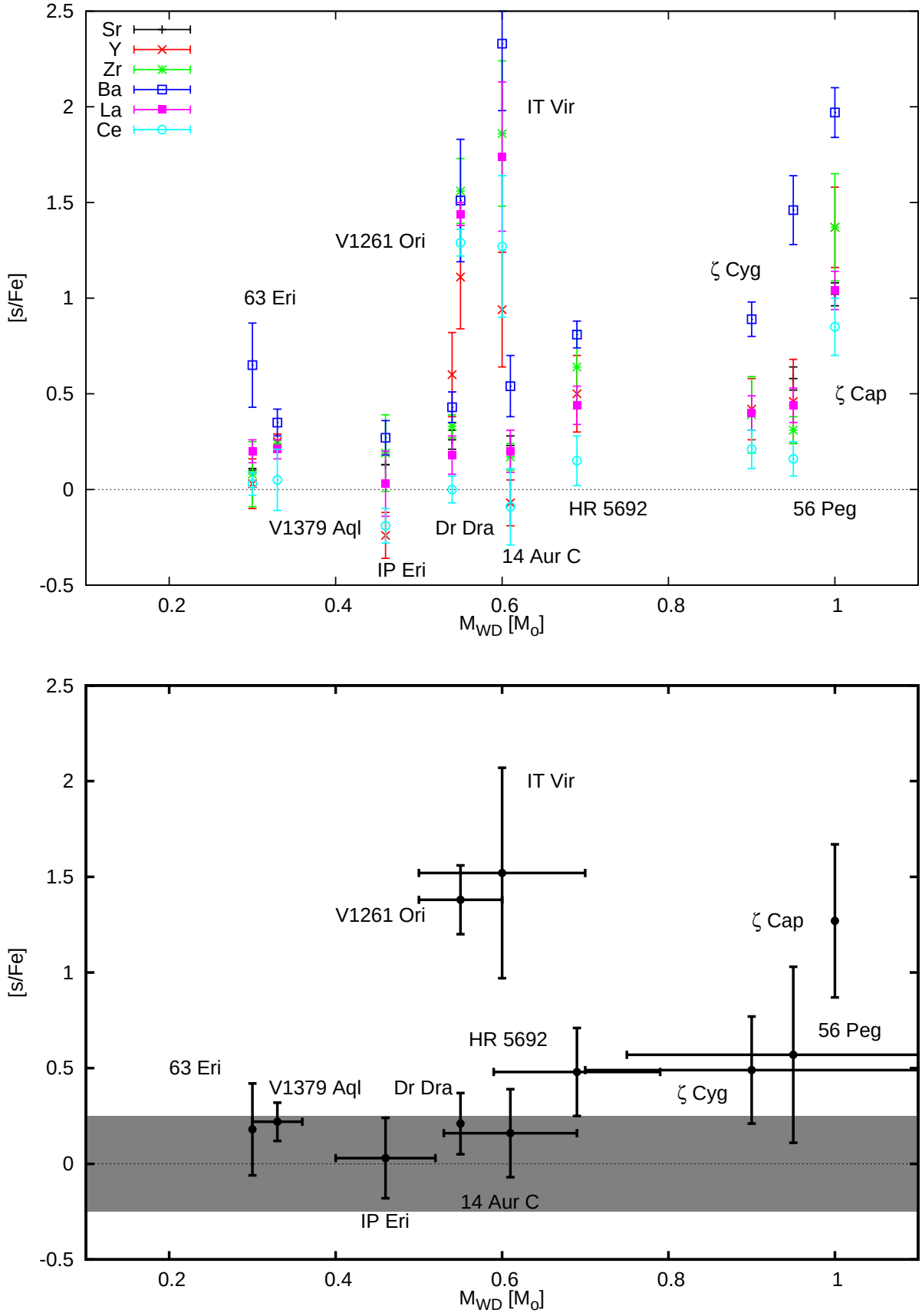

Fig. 5. Upper panel: First (Sr, Y, Zr) and second peak (Ba, La, Ce) s-process abundances relative to Fe as a function of the WD mass (a color version is available online). Lower panel: Same as left panel but with mean s-process abundances relative to Fe. To guide the eye, the grey zone marks the ±0.25 dex zone with no significant enhancement in s-process abundances.

7. Conclusion

We have analyzed a sample of 11 binary systems comprising WD of known masses. High-resolution and high-signal-to-noise spectra were collected from the HERMES spectrograph installed at the Mercator 1.2m telescope. The atmospheric parameters and the CNO and s-process abundances were derived using state-of-the-art LTE models and line lists. We derived for the first time atmospheric parameters for 14 Aur C (HD 33959C) and s-process element abundances for 56 Peg (HR 8796). The sample includes 2 S stars which have been analysed with new dedicated S-star MARCS model atmospheres. One of them, IT Vir (HD 121447), has the largest overabundance of s-process elements in the sample and has been identified as highly N-enriched. Such a high level of N overabundance could perhaps be related to the photometric variations exhibited by that star, and attributed to ellipsoidal variations as the red giant has a large Roche-filling factor. The ensuing faster rotation could trigger deep mixing which is known to bring nitrogen to the surface.

Finally, from our homogeneous study of s-process abundances in the primary components of binary systems involving a WD companion, we find that there is a clear relationship between s-process enrichment and WD mass: as expected, primary components in binary systems involving He WDs (thus with a mass lower than about 0.5 $M_{\odot}$) never show s-process overabundances, as the WD progenitor never reached the TP-AGB.

Acknowledgements. This research has been funded by the Belgian Science Policy Office under contract BR/143/A2/STARLAB. T.M. is supported by the FNRS-F.R.S. as temporary post-doctoral researcher under grant No. 2.4513.11. This work was supported by the Fonds de la Recherche Scientifique FNRS under Grant no T.0198.13. The Mercator telescope is operated thanks to grant number G.0C31.13 of the FWO under the 'Big Science' initiative of the Flemish governement. Based on observations obtained with the HERMES spectrograph, supported by the Fund for Scientific Research of Flanders (FWO), the Research Council of K.U.Leuven, the Fonds National de la Recherche Scientifique (F.R.S.-FNRS), Belgium, the Royal Observatory of Belgium, the Observatoire de Genève, Switzerland and the Thüringer Landessternwarte Tautenburg, Germany. This work has made use of the VALD database, operated at Uppsala University, the Institute of Astronomy RAS in Moscow, and the University of Vienna.

References

Abia, C. & Wallerstein, G. 1998, MNRAS, 293, 89
Ake, T. B. 1979, ApJ, 234, 538
Ake, III, T. B., Johnson, H. R., & Ameen, M. M. 1991, ApJ, 383, 842
Alvarez, R. & Plez, B. 1998, A&A, 330, 1109
Asplund, M. 2005, ARA&A, 43, 481
Böhm-Vitense, E., Carpenter, K., Robinson, R., Ake, T., & Brown, J. 2000, 533, 969
Barbuy, B., Jorissen, A., Rossi, S. C. F., & Arnould, M. 1992, A&A, 262, 216
Barisevičius, G., Tautvaišienė, G., Berdyugina, S., Chorniy, Y., & Ilyin, I. 2010, Baltic Astronomy, 19, 157
Berdyugina, S. V. 1994, Astronomy Letters, 20, 796
Bessell, M. S., Castelli, F., & Plez, B. 1998, A&A, 333, 231
Bidelman, W. P. & Keenan, P. C. 1951, 114, 473
Bilíková, J., Chu, Y.-H., Gruendl, R. A., & Maddox, L. A. 2010, AJ, 140, 1433
Böhm-Vitense, E. 1980, ApJ, 239, L79
Böhm-Vitense, E., Nemec, J., & Proffitt, C. 1984, 278, 726
Burleigh, M. R., Barstow, M. A., & Fleming, T. A. 1997, MNRAS, 287, 381
Burleigh, M. R., Barstow, M. A., & Holberg, J. B. 1998, MNRAS, 300, 511
Christian, D. J., Vennes, S., Thorstensen, J. R., & Mathioudakis, M. 1996, AJ, 112, 258
Clayton, D. D. 1988, MNRAS, 234, 1
Decressin, T., Charbonnel, C., Siess, L., et al. 2009, A&A, 505, 727
Den Hartog, E. A., Lawler, J. E., & Wood, M. P. 2014a, ApJS, 215, 7
Den Hartog, E. A., Ruffoni, M. P., Lawler, J. E., et al. 2014b, ApJS, 215, 23
Dominy, J. F. & Lambert, D. L. 1983, 270, 180
Fekel, F. C., Henry, G. W., Busby, M. R., & Eitter, J. J. 1993, AJ, 106, 2370
Fekel, F. X. & Simon, T. 1985, AJ, 90, 812
Frankowski, A. & Jorissen, A. 2006, The Observatory, 126, 25
Gray, R. O., Corbally, C. J., Garrison, R. F., McFadden, M. T., & Robinson, P. E. 2003, AJ, 126, 2048
Gray, R. O., McGahee, C. E., Griffin, R. E. M., & Corbally, C. J. 2011, AJ, 141, 160
Grevesse, N., Asplund, M., & Sauval, A. J. 2007, Space Sci. Rev., 130, 105
Griffin, R. F. 2006, The Observatory, 126, 1
Griffin, R. F. & Keenan, P. C. 1992, The Observatory, 112, 168
Gustafsson, B., Edvardsson, B., Eriksson, K., et al. 2008, A&A, 486, 951
Han, Z., Eggleton, P. P., Podsiadlowski, P., & Tout, C. A. 1995, MNRAS, 277, 1443
Herwig, F., Schoenberner, D., & Bloecker, T. 1998, A&A, 340, L43
Hoard, D. W., Wachter, S., Sturch, L. K., et al. 2007, AJ, 134, 26
Holweger, H. 1979, in Liege International Astrophysical Colloquia, Vol. 22, Liege International Astrophysical Colloquia, ed. A. Boury, N. Grevesse, & L. Remy-Battiau, 117–138
Hurley, J. R., Pols, O. R., & Tout, C. A. 2000, MNRAS, 315, 543
Jeffries, R. D. & Smalley, B. 1996, A&A, 315, L19
Jofre, P., Heiter, U., Soubiran, C., et al. 2013, ArXiv e-prints
Johnson, J. A. 2002, ApJS, 139, 219
Jorissen, A. & Boffin, H. M. J. 1992, in Binaries as Tracers of Stellar Formation, ed. A. Duquennoy & M. Mayor (Cambridge: Cambridge University Press), 110
Jorissen, A., Hennen, O., Mayor, M., Bruch, A., & Sterken, C. 1995, A&A, 301, 707
Jorissen, A., Mayor, M., Manfroid, J., & Sterken, C. 1992, Information Bulletin on Variable Stars, 3730, 1
Jorissen, A., Schmitt, J. H. M. M., Carquillat, J. M., Ginestet, N., & Bickert, K. F. 1996, A&A, 306, 467
Jorissen, A., Van Eck, S., Mayor, M., & Udry, S. 1998, A&A, 332, 877
Käppeler, F., Gallino, R., Bisterzo, S., & Aoki, W. 2011, Rev. Mod. Phys., 83, 157
Kovacs, N. 1983, A&A, 120, 21
Kupka, F., Dubernet, M.-L., & VAMDC Collaboration. 2011, Baltic Astronomy, 20, 503
Landsman, W., Simon, T., & Bergeron, P. 1993, PASP, 105, 841
Lucatello, S., Gratton, R., Cohen, J. G., et al. 2003, AJ, 125, 875
Masseron, T. 2006, PhD thesis, Observatoire de Paris
Masseron, T., Plez, B., Van Eck, S., et al. 2014, A&A, in press
McClure, R. D., Fletcher, J. M., & Nemec, J. M. 1980, 238, L35
McClure, R. D. & Woodsworth, A. W. 1990, 352, 709
Merle, T., Jorissen, A., Masseron, T., et al. 2014, A&A, 567, A30
Neyskens, P., van Eck, S., Jorissen, A., et al. 2015, Nature, 517, 174
Olshevsky, V. L. & Shchukina, N. G. 2007, in Modern solar facilities - advanced solar science, ed. F. Kneer, K. G. Puschmann, & A. D. Wittmann, 307
Plez, B. 2012, Astrophysics Source Code Library, 5004
Pols, O. R., Karakas, A. I., Lattanzio, J. C., & Tout, C. A. 2003, in Astronomical Society of the Pacific Conference Series, Vol. 303, Symbiotic Stars Probing Stellar Evolution, ed. R. L. M. Corradi, J. Mikolajewska, & T. J. Mahoney, 290
Prugniel, P., Vauglin, I., & Koleva, M. 2011, A&A, 531, A165
Raskin, G., van Winckel, H., Hensberge, H., et al. 2011, A&A, 526, A69
Ricker, P. M. & Taam, R. E. 2008, ApJ, 672, L41
Ruffoni, M. P., Den Hartog, E. A., Lawler, J. E., et al. 2014, MNRAS, 441, 3127
Schindler, M., Stencel, R. E., Linsky, J. L., Basri, G. S., & Helfand, D. J. 1982, 263, 269
Siess, L., Davis, P. J., & Jorissen, A. 2014, A&A, 565, A57
Smiljanic, R., Porto de Mello, G. F., & da Silva, L. 2007, A&A, 468, 679
Smith, V. V. 1984, A&A, 132, 326
Smith, V. V. & Lambert, D. L. 1990, ApJS, 72, 387
Sneden, C., Lucatello, S., Ram, R. S., Brooke, J. S. A., & Bernath, P. 2014, ApJS, 214, 26
Stefanik, R. P., Torres, G., Latham, D. W., et al. 2011, AJ, 141, 144
Theuns, T., Boffin, H. M. J., & Jorissen, A. 1996, MNRAS, 280, 1264
Van Eck, S., Neyskens, P., Plez, B., et al. 2011, Journal of Physics Conference Series, 328, 012009
van Leeuwen, F. 2007, A&A, 474, 653
Vennes, S., Christian, D. J., Mathioudakis, M., & Doyle, J. G. 1997, A&A, 318, L9
Vennes, S., Christian, D. J., & Thorstensen, J. R. 1998, ApJ, 502, 763
Vennes, S., Mathioudakis, M., Doyle, J. G., Thorstensen, J. R., & Byrne, P. B. 1995, A&A, 299, L29
Zacs, L., Musaev, F. A., Bikmaev, I. F., & Alksnis, O. 1997, A&AS, 122, 31

Appendix A: Atomic linelist

Table A.1. Atomic line list. A vertical mark spanning different spectral lines identify hyperfine or isotopic components.

λ [nm]	χ [eV]	$\log gf$	
C I	$A_\odot$(C) = 8.39		
538.0337	7.685	−1.615	
555.3174	8.643	−2.370	
768.5190	8.771	−1.519	
833.5148	7.685	−0.420	
872.7126	1.264	−8.136	
O I	$A_\odot$(O) = 8.66		
615.6776	10.741	−0.694	
630.0304	0.000	−9.715	
636.3776	0.020	−10.190	
777.1941	9.146	0.369	only in IT Vir
777.4161	9.146	0.223	only in IT Vir
777.5388	9.146	0.001	only in IT Vir
844.6359	9.521	0.236	
844.6758	9.521	0.014	
Sr I	$A_\odot$(Sr) = 2.92		
460.7327	0.000	0.283	NIST AA
640.8459	2.271	0.510	in the red wing of a Fe I line
687.8310	1.798	−0.240	only in V1261 Ori
689.2581	0.000	−2.840	only in V1261 Ori
707.0070	1.847	−0.030	
Sr II	$A_\odot$(Sr) = 2.92		
407.7719	0.000	0.170	only in 14 Aur C
416.1792	2.940	−0.600	only in 14 Aur C and 63 Eri
421.5519	0.000	−0.170	only in 14 Aur C
Y I	$A_\odot$(Y) = 2.21		
563.0130	1.356	0.211	only in IT Vir
613.8435	0.066	−1.923	
622.2578	0.000	−1.452	
640.2006	0.066	−1.849	only in 56 Peg and IT Vir
643.5004	0.066	−0.820	
668.7567	0.000	−2.000	only in V1261 Ori
Y II	$A_\odot$(Y) = 2.21		
395.0352	0.104	−0.490	only in 14 Aur C
488.3684	1.084	0.265	only in 14 Aur C and V1379 Aql
490.0120	1.033	0.103	only in IP Eri
508.7416	1.084	−0.170	
520.0406	0.992	−0.570	
528.9815	1.033	−1.850	
532.0782	1.084	−1.950	only in V1379 Aql
540.2774	1.839	−0.630	
554.4611	1.738	−1.090	only in 63 Eri and V1379 Aql
554.6009	1.748	−0.754	
566.2925	1.944	0.384	
572.8890	1.839	−1.120	
661.3733	1.748	−0.848	
679.5414	1.738	−1.030	
788.1881	1.839	−0.570	
Zr I	$A_\odot$(Zr) = 2.58		
473.9480	0.651	0.230	only in 63 Eri
477.2323	0.623	0.040	

Table A.1. Continued.

λ [nm]	χ [eV]	log gf	
488.7750	0.730	1.000	
538.5151	0.519	−0.710	
568.0.92	0.543	−1.700	only in IT Vir
573.5690	0.000	−2.240	only in ζ Cap
612.7475	0.154	−1.060	
613.4585	0.000	−1.280	
614.0535	0.519	−1.410	
614.3252	0.071	−1.100	
644.5747	0.999	−0.830	
650.6437	0.633	−2.110	only in ζ Cap
699.0869	0.623	−1.220	
709.7774	0.687	−0.570	only in V1379 Aql
716.9130	0.730	−0.880	
733.6066	0.519	−2.170	only in IT Vir
743.9889	0.543	−1.810	
755.3039	0.519	−3.040	only in V1261 Ori
755.4780	0.520	−2.280	only in V1261 Ori
755.8487	1.550	−1.470	only in V1261 Ori
760.7167	0.633	−1.880	
784.9365	0.687	−1.300	
805.8107	0.623	−2.020	only in IT Vir
806.3105	0.623	−1.620	only in ζ Cap
807.0115	0.730	−0.790	only in IP Eri and IT Vir
813.3011	0.687	−1.130	only in ζ Cap and IT Vir
846.4687	0.651	−2.080	only in IT Vir
Zr II	$A_\odot$(Zr) = 2.58		
4150.986	0.802	−0.992	only in 14 Aur C
4211.877	0.527	−1.040	only in 14 Aur C
4379.742	1.532	−0.356	only in 14 Aur C
5112.270	1.665	−0.850	
5350.350	1.773	−1.160	
5418.016	1.756	−1.600	only in HR5692
Ba I	$A_\odot$(Ba) = 2.17		
748.8077	1.190	−0.230	
Ba II	$A_\odot$(Ba) = 2.17		
389.1776^{134}	2.512	0.295	
389.1776^{135}	2.512	0.295	
389.1776^{136}	2.512	0.295	Only in HR5692
389.1776^{137}	2.512	0.295	
389.1776^{138}	2.512	0.295	
416.6000^{134}	2.722	−0.433	
416.6000^{135}	2.722	−0.433	
416.6000^{136}	2.722	−0.433	Only in DR Dra
416.6000^{137}	2.722	−0.433	
416.6000^{138}	2.722	−0.433	
452.4925^{130}	2.512	−0.390	
452.4925^{132}	2.512	−0.390	
452.4925^{134}	2.512	−0.390	
452.4925^{135}	2.512	−0.390	Only in 63 Eri
452.4925^{136}	2.512	−0.390	
452.4925^{137}	2.512	−0.390	
452.4925^{138}	2.512	−0.390	
455.3998^{137}	0.000	−0.666	
455.3999^{137}	0.000	−0.666	

Table A.1. Continued.

λ [nm]	χ [eV]	$\log gf$	
455.4000[137]	0.000	−1.064	
455.4001[135]	0.000	−0.666	
455.4002[135]	0.000	−1.064	
455.4002[135]	0.000	−0.666	
455.4031[130]	0.000	0.140	
455.4031[132]	0.000	0.140	
455.4031[134]	0.000	0.140	Only in 14 Aur C and V1379 Aql
455.4032[136]	0.000	0.140	
455.4033[138]	0.000	0.140	
455.4048[135]	0.000	−0.219	
455.4050[135]	0.000	−0.666	
455.4051[137]	0.000	−0.219	
455.4052[135]	0.000	−1.365	
455.4054[137]	0.000	−0.666	
455.4055[137]	0.000	−1.365	
493.4030[137]	0.000	−0.662	
493.4032[135]	0.000	−0.662	
493.4042[135]	0.000	−1.361	
493.4042[137]	0.000	−1.361	
493.4074[130]	0.000	−0.157	
493.4074[132]	0.000	−0.157	
493.4074[134]	0.000	−0.157	Only in 14 Aur C
493.4075[136]	0.000	−0.157	
493.4077[138]	0.000	−0.157	
493.4091[135]	0.000	−0.662	
493.4095[137]	0.000	−0.662	
493.4102[135]	0.000	−0.662	
493.4107[137]	0.000	−0.662	
585.3669[135]	0.604	−1.967	
585.3669[137]	0.604	−1.967	
585.3670[135]	0.604	−2.113	
585.3670[135]	0.604	−1.909	
585.3671[137]	0.604	−2.113	
585.3671[137]	0.604	−1.909	
585.3672[135]	0.604	−2.113	
585.3672[135]	0.604	−2.511	
585.3673[130]	0.604	−0.909	
585.3673[132]	0.604	−0.909	
585.3673[134]	0.604	−0.909	
585.3673[137]	0.604	−2.113	
585.3673[135]	0.604	−1.812	
585.3673[137]	0.604	−2.511	
585.3674[136]	0.604	−0.909	
585.3675[135]	0.604	−1.909	
585.3675[135]	0.604	−1.365	
585.3675[137]	0.604	−1.812	
585.3675[138]	0.604	−0.909	
585.3676[137]	0.604	−1.909	
585.3676[137]	0.604	−1.365	
585.3680[135]	0.604	−1.967	
585.3682[137]	0.604	−1.967	
614.1708[135]	0.704	−0.456	
614.1708[135]	0.704	−1.264	
614.1709[135]	0.704	−2.410	
614.1709[137]	0.704	−1.264	

Table A.1. Continued.

λ [nm]	χ [eV]	log gf	
614.1709^{137}	0.704	−0.456	
614.1710^{137}	0.704	−2.410	
614.1711^{130}	0.704	−0.030	
614.1711^{132}	0.704	−0.030	
614.1711^{134}	0.704	−0.030	
614.1712^{136}	0.704	−0.030	
614.1713^{135}	0.704	−0.662	
614.1713^{138}	0.704	−0.030	
614.1714^{135}	0.704	−1.167	
614.1715^{135}	0.704	−2.234	
614.1715^{137}	0.704	−0.662	
614.1716^{135}	0.704	−0.912	
614.1716^{137}	0.704	−1.167	
614.1717^{135}	0.704	−1.234	
614.1717^{135}	0.704	−1.280	
614.1717^{137}	0.704	−2.234	
614.1718^{137}	0.704	−0.912	
614.1719^{137}	0.704	−1.234	
614.1719^{137}	0.704	−1.280	
649.6883^{135}	0.604	−1.911	
649.6883^{137}	0.604	−1.911	
649.6888^{135}	0.604	−1.212	
649.6888^{137}	0.604	−1.212	
649.6895^{130}	0.604	−0.406	
649.6895^{132}	0.604	−0.406	
649.6895^{134}	0.604	−0.406	
649.6895^{135}	0.604	−0.765	
649.6896^{137}	0.604	−0.765	
649.6897^{136}	0.604	−0.406	
649.6898^{138}	0.604	−0.406	
649.6900^{135}	0.604	−1.610	
649.6902^{135}	0.604	−1.212	
649.6902^{137}	0.604	−1.610	
649.6904^{137}	0.604	−1.212	
649.6906^{135}	0.604	−1.212	
649.6909^{137}	0.604	−1.212	
La II	$A_\odot$(La) = 1.13		
394.9037	0.403	−1.337	
394.9038	0.403	−1.191	
394.9044	0.403	−0.995	
394.9046	0.403	−1.008	
394.9047	0.403	−1.668	
394.9056	0.403	−0.761	
394.9058	0.403	−0.886	
394.9059	0.403	−1.559	
394.9072	0.403	−0.576	
394.9075	0.403	−0.825	Only in 14 Aur C
394.9077	0.403	−1.580	
394.9093	0.403	−0.420	
394.9097	0.403	−0.821	
394.9100	0.403	−1.690	
394.9120	0.403	−0.284	
394.9124	0.403	−0.887	
394.9127	0.403	−1.902	
394.9151	0.403	−0.163	
394.9156	0.403	−1.092	
394.9160	0.403	−2.305	

Table A.1. Continued.

λ [nm]	χ [eV]	$\log gf$	
398.8445	0.403	−1.362	
398.8446	0.403	−1.839	
398.8452	0.403	−1.140	
398.8454	0.403	−1.362	
398.8464	0.403	−1.041	
398.8466	0.403	−1.985	
398.8467	0.403	−1.140	
398.8482	0.403	−1.015	
398.8484	0.403	−1.355	
398.8486	0.403	−1.041	Only in 63 Eri
398.8504	0.403	−1.068	
398.8507	0.403	−0.969	
398.8509	0.403	−1.015	
398.8532	0.403	−1.263	
398.8535	0.403	−0.683	
398.8538	0.403	−1.068	
398.8569	0.403	−0.455	
398.8572	0.403	−1.263	
404.2901	0.927	0.290	Only in 63 Eri
408.6695	0.000	−1.266	
408.6699	0.000	−1.108	
408.6702	0.000	−1.119	
408.6705	0.000	−1.292	
408.6708	0.000	−0.696	
408.6709	0.000	−1.094	
408.6710	0.000	−1.790	Only in HR 5692
408.6711	0.000	−1.468	
408.6711	0.000	−3.216	
408.6717	0.000	−1.292	
408.6719	0.000	−1.119	
408.6720	0.000	−1.108	
408.6721	0.000	−1.266	
466.2478	0.000	−2.952	
466.2482	0.000	−2.511	
466.2486	0.000	−2.240	
466.2491	0.000	−2.253	
466.2492	0.000	−2.137	
466.2493	0.000	−2.256	
466.2503	0.000	−2.511	
466.2505	0.000	−2.056	
466.2507	0.000	−1.763	
474.8726	0.927	−0.540	Only in ζ Cyg and 63 Eri
480.4039	0.235	−1.490	Only in 56 Peg and IT vir
492.1774	0.244	−1.139	
492.1774	0.244	−2.220	
492.1774	0.244	−3.601	
492.1775	0.244	−1.233	
492.1775	0.244	−2.005	
492.1775	0.244	−3.207	
492.1776	0.244	−1.334	
492.1776	0.244	−1.445	
492.1776	0.244	−1.915	
492.1776	0.244	−1.927	
492.1776	0.244	−2.923	Only in ζ Cap et 14 Aur C
492.1776	0.244	−3.010	

Table A.1. Continued.

λ [nm]	χ [eV]	$\log gf$	
492.1777	0.244	−1.566	
492.1777	0.244	−1.955	
492.1777	0.244	−2.939	
492.1778	0.244	−1.700	
492.1778	0.244	−1.848	
492.1778	0.244	−2.006	
492.1778	0.244	−2.053	
492.1778	0.244	−2.258	
492.1778	0.244	−3.123	
511.4559	0.235	−1.030	Only in 14 Aur C
529.0818	0.000	−1.650	
530.1908	0.403	−3.065	
530.1913	0.403	−2.266	
530.1917	0.403	−2.391	
530.1946	0.403	−3.483	
530.1953	0.403	−2.300	
530.1958	0.403	−2.120	
530.2001	0.403	−2.483	
530.2008	0.403	−1.913	
530.2067	0.403	−1.742	
530.3513	0.321	−1.874	
530.3513	0.321	−2.363	
530.3514	0.321	−3.062	
530.3531	0.321	−2.167	
530.3532	0.321	−2.247	
530.3532	0.321	−2.622	
530.3546	0.321	−2.366	
530.3546	0.321	−2.622	
530.3547	0.321	−2.351	
580.5773	0.126	−1.560	
586.3691	0.927	−1.370	Only in ζ Cap
593.6210	0.173	−2.070	
617.2721	0.126	−2.253	
626.2422	0.403	−1.873	
626.2429	0.403	−2.802	
626.2434	0.403	−4.015	
639.0455	0.321	−2.012	
639.0468	0.321	−2.183	
639.0468	0.321	−2.752	
639.0479	0.321	−2.570	
639.0479	0.321	−3.752	
639.0480	0.321	−2.390	
639.0489	0.321	−2.536	
639.0489	0.321	−3.334	
639.0490	0.321	−2.661	
639.0496	0.321	−3.100	
639.0497	0.321	−2.595	
639.0498	0.321	−3.079	
639.0502	0.321	−2.954	
639.0503	0.321	−2.778	
639.0506	0.321	−2.857	
677.4268	0.126	−1.708	
683.4099	0.244	−2.168	Only in ζ Cap and 56 Peg
706.6198	0.000	−1.655	Only in IP Eri and DR Dra

Table A.1. Continued.

λ [nm]	χ [eV]	$\log gf$	
748.3490	0.126	−1.891	
Ce II	$A_\odot$(Ce) = 1.70		
434.9768	0.529	−0.520	
434.9789	0.701	−0.350	
451.5848	1.058	−0.240	Only in ζ Cyg and HR 5692
456.2359	0.478	0.230	
462.8239	1.366	−0.430	
477.3941	0.924	−0.390	Only in ζ Cap
494.3441	1.206	−0.360	
494.4618	1.008	−0.520	Only in ζ Cap
518.7503	0.559	−3.330	
527.4229	1.044	0.130	Only in ζ Cap and 14 Aur C
533.0556	0.869	−0.400	
5472.279	1.247	−0.100	Only in 63 Eri
597.5818	1.327	−0.460	Only in IP Eri
597.5881	1.251	−1.680	and HR 5692
604.3373	1.206	−0.480	
605.1815	0.232	−1.530	
605.2617	1.838	−0.800	Only in ζ Cap
758.0913	0.327	−2.120	Only in V1261 Ori
802.5571	0.000	−1.420	
871.6659	0.122	−1.980	
877.2135	0.357	−1.260	
891.0948	0.435	−1.800	
897.0176	0.295	−2.020	Only in V1261 Ori
899.3403	0.265	−2.520	Only in V1261 Ori

Appendix B: Molecular linelist

Table B.1. Molecular linelist.

λ [nm]	comments
C_2	
468.427	only used for 14 Aur C
471.30	
473.277	
473.50	
473.531	
489.748	region difficult to fit
493.667	
495.142	
495.60	
496.363	
502.416	
503.36	
505.88	
506.672	
507.35	
507.528	
508.92	
513.56	used in Barbuy et al. (1992)
514.12	
558.52	
562.12	
CN	
639.63	
642.07	
645.85	

Table B.1. Continued.

λ [nm]
647.72
651.97
653.56
654.90
696.19
697.42
700.91
700.96
701.19
720.52
723.81
726.36
733.70
734.01
734.06
734.23
737.45
738.45
739.79
740.34
745.63
749.92
753.95
754.91
757.19
787.40
789.21
790.67
790.96
791.18
792.30
792.97
793.86
793.92
795.17
795.41
795.82
796.71
797.08
797.38
797.47
797.72
797.98
798.11
798.46
798.52
799.23
799.56
800.85
801.57
801.70
801.81
803.28
803.50
803.81
804.17
805.31
805.73
806.41
807.44
808.25

Table B.1. Continued.

λ [nm]
808.62
808.73
808.83
810.04
810.15
811.87
812.40
812.56
813.21
816.01
816.69
817.51
818.02
820.70
823.60
824.73
826.72
826.80
829.12
831.24
832.55
833.04
833.74
835.07
837.15
839.12
839.85
840.72
841.13
842.05
842.24
843.00
843.12
844.18
845.78
846.99
847.09
847.24
847.84
850.51
852.34
856.70
857.33
857.72
858.70
860.49
860.77
862.05
862.44
863.00
862.91
870.31
870.68
875.97
881.62
881.79
884.19